Proceedings of the Seventh International Conference on
Railway Technology: Research, Development and Maintenance
Edited by: J. Pombo
Civil-Comp Conferences, Volume 15, Paper 11.3
Civil-Comp Press, Edinburgh, United Kingdom, 2026
ISSN: 2753-3239, doi: 10.4203/ccc.15.11.3

Robust Current Control for High-Speed Maglev Based on Three Step Power Supply Switching Method

W. Chen[1,2], Q. Ge[1,2], J. Zhu[1,2], M. Zhao[1,2] and L. Zhao[1,2]

[1]Key Laboratory of High Density Electromagnetic Power and Systems , Institute of Electrical Engineering, Chinese Academy of Sciences, Beijing, China
[2]University of Chinese Academy of Sciences, Beijing, China

Abstract

The high-speed maglev train is driven by long stator linear synchronous motor (LS-LSM). To reduce active power loss and improve motor operation efficiency, the stator segments of the LS-LSM adopt a segmented power supply mode. However, during the changeover process of the motor, a multi-parameter perturbation phenomenon occurs in the motor parameters, which in turn affects the control accuracy and stability of the current loop. In this study, first, with the aid of finite element software, the multi-parameter time-varying characteristics of the motor during changeover process are thoroughly analyzed, and the motor mathematical model under the three-step switching method is established. Second, to address the disturbance problem of the current loop caused by multi-parameter perturbations and enhance the robustness of the current loop, the active disturbance rejection control (ADRC) strategy based on the high-order extended state observer (HESO) is proposed. Finally, verification tests are carried out on the high-speed maglev simulation model with three-step switching method. The results show that the proposed algorithm can effectively suppress the impact of parameter perturbations, verifying its effectiveness and feasibility.

Keywords: high-speed maglev, long stator linear synchronous motor, three step power supply switching method, current loop control, high order extend state observer, active disturbance rejection control.

1 Introduction

At present, traditional high-speed railway transportation is limited by various factors such as wheel-rail adhesion and pantograph-catenary current collection, making it difficult to significantly increase the speed. The conventional high-speed maglev train is driven by the LS-LSM and relies on the attractive force of suspension electromagnets to make the train suspend above the track. This overcomes the defects of wheel-rail trains and achieves a significant improvement in speed[1],[2]. The maglev contains two LS-LSMs, which are composed of stators and movers on the left and right sides of the track. The stators of the LS-LSM are segmented every 1200 meters, with no electrical connection between each stator segment. When the train crosses different stator segments, the power supply switching methods for the exiting and entering stator segments include the frog-leap method, two-step method, three-step method, etc. In the frog-leap method, the tracks on both left and right sides enter the changeover simultaneously, resulting in a jump in traction during the power supply switching process. Currently, the mainstream method is the two-step switching method, where the stators on both sides of the track are arranged in a staggered manner. During the switching process, the stator segment on the exiting side of the train needs to gradually reduce the current to 0 before restoring the power supply to the entering side stator segment, and the traction loss caused in this process reaches 50%.

However, when the train is running at high speed, the frequent occurrence of changeover operations will lead to continuous traction loss, which has an adverse impact on both the speed-up performance and operation stability of the train. Compared with the two-step method, the three-step method requires additional converters, which no longer supply power only to the track on one side but follow the rule of taking 6 stator segments as one power supply cycle. Nevertheless, it can shorten the speed-up time, as the stators on both sides of the track are always in the driving state, and there is no traction loss during the changeover process.Figure 1 shows the connection diagram of the three-step switching method. In the single-feeding (SF) mode, only two converters on the left or right side supply power to the stator segments when the train is not in the step change stage; during the changeover process, all converters on one side are activated. In the double-feeding (DF) mode, the number of converters put into operation under all working conditions is twice that of the SF mode. During the changeover process, differences in the electromagnetic coupling area between the mover and different stator segments lead to dynamic changes in multiple motor parameters, which deteriorates the dynamic and steady-state performance of the current loop.

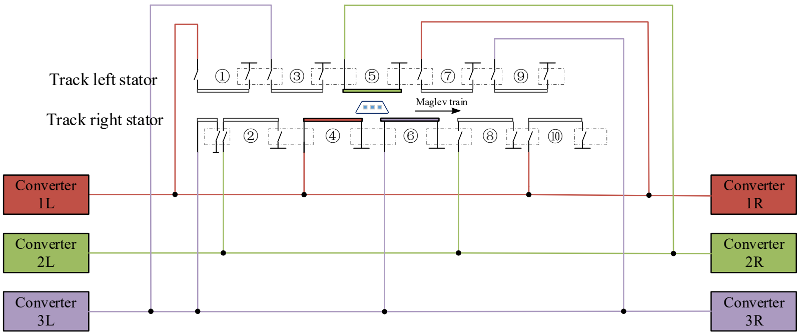

Figure 1： Connection diagram of three-step power supply switching method.

To cope with the disturbances caused by parameter time-varying, an effective approach is to optimize the current loop control strategy. Common methods include proportional-integral control[3], sliding mode control[4], deadbeat current control[5], and active disturbance rejection control (ADRC)[6]. The initial ADRC was first proposed by Han in 1998. As the core of ADRC, the extended state observer (ESO) can estimate and compensate for the total disturbances in the system, thereby achieving stronger anti-disturbance performance. However, nonlinear parameters increase the difficulty of algorithm design and limit its application. To solve this problem, linear ADRC was proposed in [7], and it has been more widely applied in motor control. At present, numerous scholars have carried out extensive research work on ADRC. In the traditional ADRC framework, it is difficult for ESO to achieve accurate observation of fast-varying periodic disturbances; one type of improved method embeds the periodic signal internal model into the ADRC framework, which can effectively improve its harmonic disturbance suppression performance[8]. Another type of improved method constructs a high-order extended state observer (HESO) by increasing the order of ESO[10], which achieves asymptotic convergence of high-order terms in the polynomial form of disturbances, thereby improving the estimation accuracy of time-varying disturbances. Compared with the first type of method, the design of HESO requires less disturbance information, so it is insensitive to frequency changes and has strong anti-disturbance capability.

This paper proposes an enhanced ADRC current loop control strategy based on the HESO to cope with the parameter time-varying disturbances caused by motor changeover. The remaining parts of this paper are arranged as follows: Section II successfully establishes a three-dimensional(3D) finite element model of the LS-LSM and analyzes the parameter time-varying characteristics during the motor changeover process. Section III establishes the motor mathematical model under the three-step switching method. Section IV introduces the current loop control based on the improved ADRC adopted in this paper. Section V successfully verifies the effectiveness of the proposed algorithm through simulation. Finally, Section VI concludes this article.

2 Time-Varying Characteristics of Motor Parameters During the Changeover Process of LS-LSM

As the mover, the train has a significant difference between its body length and the stator length. Usually, the stator length is much larger than the train body length. Therefore, the stator segments can be divided into different regions, as shown in Figure 2. The LS-LSM includes the full marshalling train and stator segments, so the *dq*-axis inductances of the motor consist of two parts: one part is the inductance coupled between the mover excitation poles in the covered area and the stator windings, and the other part is the inductance of the stator windings in the uncovered area that is not coupled with the mover excitation poles. The expressions of the *dq*-axis inductances are

$$L_{ds} = L_{dis} + L_{dos},\ L_{qs} = L_{qis} + L_{qos} \tag{1}$$

where L_{dis} and L_{qis} are the *d- and q*-axis inductances in the covered area, L_{dos} and L_{qos} are the *d*- and *q*-axis inductances in the uncovered area, L_{ds} and L_{qs} are the *d- and q*-axis total inductances.

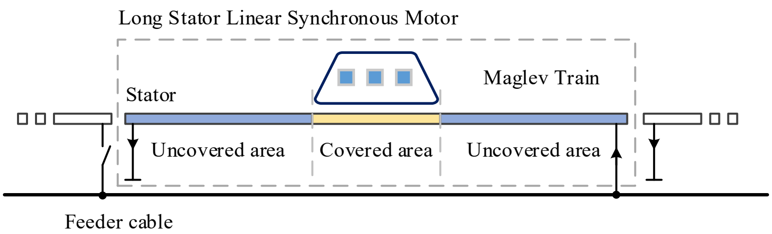

Figure 2: Schematic diagram of stator section area division

The stator of the LS-LSM is powered in segments. Trackside switchgears corresponding to the specific stator segments are only closed to supply power when the train passes through. In the three-step switching method, the mover couples with two stator segments simultaneously during the changeover process. Since both stator segments are energized, this scenario can be equivalent to two motors providing traction force to the train jointly. A single train consist of the high-speed maglev is composed of multiple motor units. Figure 3 shows the 3D finite element model of the LS-LSM unit, where the stator segment is extended to simulate the motor changeover. As the train departs from a stator segment, the coupling area between the stator and the mover gradually decreases, leading to a reduction in the motor self-inductances and mutual inductances. Conversely, when the train enters a new stator segment, the coupling area increases progressively, resulting in higher self-inductances and mutual inductances. Figure 4 shows the variation curves of the self-inductances and mutual inductances of different motors during changeover. Specifically, L_{AA1} and L_{AA2} are the phase-A self-inductances of Motor 1 and Motor 2, respectively, while M_{A1N} and M_{A2N} are the mutual inductances between the stator phase-A windings and the mover for Motor 1 and Motor 2, respectively.

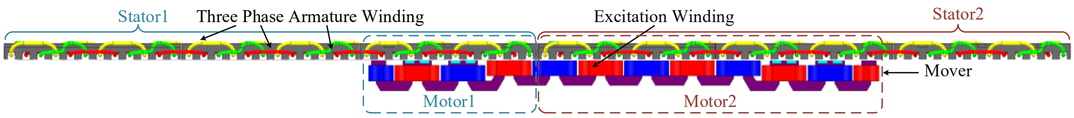

Figure 3: Three-dimensional finite element model of LS-LSM unit.

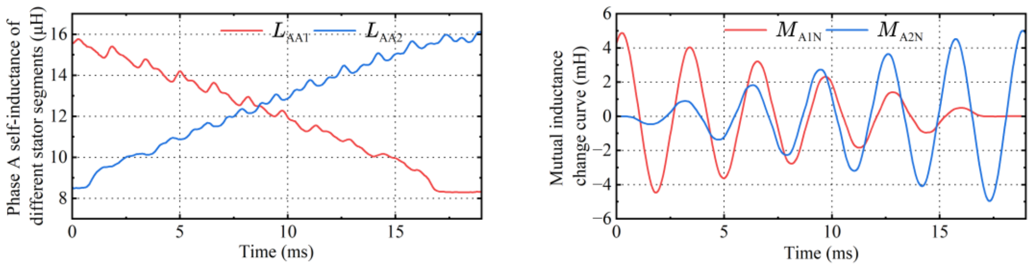

(a) (b)

Figure 4: Changes of self-inductance and mutual inductance of different motors during changeover process.

In the finite element model, the stator segment length of the motor unit is set to 3.096 m, and the mover operates at a speed of 600 km/h. The total time required for the mover to completely depart from Stator 1 is 18.57ms. Therefore, as illustrated in Figure 4 (b), the mutual inductance amplitude reaches its peak when the mover is fully coupled with Stator 1. As the mover continues to travel, the coupling area gradually decreases, leading to a synchronous reduction in the mutual inductance amplitude. At 18.57ms on the time axis, the mutual inductance amplitude decays to zero, indicating that the mover has completely left Stator 1. It can be observed that the rate of change of the motor self-inductance and mutual inductance is closely related to the train speed and stator segment length, exhibiting an approximately linear relationship. Consequently, the coupling coefficient P_c between the mover and the stator segment during the mover's departure can be calculated based on the total train length and the absolute position of the train on the track

$$P_c = \frac{al_s - S}{L_M} \tag{2}$$

where S is the absolute position of the train on the track, a is the number of the stator section, and L_M is the length of the train.

The coupling coefficient P_c is incorporated into the parameter characterization of the different motors during changeover. As the train departs from a stator segment, the stator-mover coupling area decreases gradually. Consequently, the corresponding parameters expression for Motor 1 are given by

$$L_{ds1} = P_c L_{dis} + L_{dos},\ L_{qs1} = P_c L_{qis} + L_{qos},\ \psi_{m1} = P_c \psi_m = P_c M_{sm} I_m \tag{3}$$

where L_{ds1} and L_{qs1} are the d- and q-axis inductances of Motor1, ψ_{m1} is the excitation flux of Motor1, M_{sm} is the mutual inductance of Motor1, I_m is the excitation current.

Conversely, as the train enters a subsequent stator segment, the stator-mover coupling area increases gradually. Accordingly, the corresponding parameters expression for Motor 2 are given by

$$L_{ds2}=(1-P_c)L_{dis}+L_{dos},\ L_{qs2}=(1-P_c)L_{qis}+L_{qos},\ \psi_{m2}=(1-P_c)\psi_m \tag{4}$$

where L_{ds2} and L_{qs2} are the d- and q-axis inductances of Motor2, ψ_{m2} is the excitation flux of Motor 2.

3 Mathematical Models of the Motor Under Different Operating States

When the speed of the train is lower than 56 km/h, the traction power supply system operates in the SF mode, the mathematical model of the LS-LSM in a synchronous (d, q) reference frame can be expressed as

$$\begin{bmatrix} u_d \\ u_q \end{bmatrix}=\begin{bmatrix} R_s+R_k+pL_{ds}+pL_k & -\omega_e L_{qs}-\omega_e L_k \\ \omega_e L_{qs}+\omega_e L_k & R_s+R_k+pL_{ds}+pL_k \end{bmatrix}\cdot\begin{bmatrix} i_d \\ i_q \end{bmatrix}+ \begin{bmatrix} 0 \\ (\omega_e i_d-pi_q)(L_{ds}-L_{qs})+\omega_e\psi_m \end{bmatrix} \tag{5}$$

where u_d and u_q are the d- and q-axis voltage, i_d and i_q are the d- and q-axis current, R_{s} is the stator Resistance, R_{k} and L_{k} are the resistance and inductance of the feeder cable, ω_e is the electrical angular speed of mover, p is the differential operator.

When the train speed is greater than 56 km/h, the traction power supply system enters the DF mode. A traction converter is added at the other end of the train operation line. The two converters are connected in parallel and then feed to the LS-LSM together with current sharing method through the double feeder cables. When the train operates in the DF mode, the mathematical model of the LS-LSM in a synchronous reference frame can be expressed as

$$\boldsymbol{u}_{\boldsymbol{dq}4}=\boldsymbol{A}_{\boldsymbol{dq}4}\boldsymbol{i}_{\boldsymbol{dq}4}+\boldsymbol{E}_{\boldsymbol{dq}4} \tag{6}$$

$$\boldsymbol{A}_{\boldsymbol{dq}4}=\begin{bmatrix} (R_{k1}+R_s)+(L_{ds}+L_{k1})p & -\omega_e L_{qs}-\omega_e L_{k1} & R_s+L_{ds}p & -\omega_e L_{qs} \\ \omega_e L_{qs}+\omega_e L_{k1} & (R_{k1}+R_s)+(L_{ds}+L_{k1})p & \omega_e L_{ds} & R_{\mathrm{s}}+L_{qs}p \\ R_s+L_{ds}p & -\omega_e L_{qs} & (R_{k2}+R_s)+(L_{ds}+L_{k2})s & -\omega_e(L_{qs}+L_{k2}) \\ \omega_e L_{ds} & R_s+L_{qs}p & \omega_e(L_{qs}+L_{k2}) & (R_{k2}+R_s)+(L_{ds}+L_{k2})p \end{bmatrix}$$

$$\boldsymbol{u}_{\boldsymbol{dq}4}=\begin{bmatrix} u_{d1} \\ u_{q1} \\ u_{d2} \\ u_{q2} \end{bmatrix},\boldsymbol{i}_{\boldsymbol{dq}4}=\begin{bmatrix} i_{d1} \\ i_{q1} \\ i_{d2} \\ i_{q2} \end{bmatrix},\boldsymbol{E}_{\boldsymbol{dq}4}=\begin{bmatrix} 0 \\ \omega_e\psi_m+(L_{ds}-L_{qs})(\omega_e i_{d1}-pi_{q1}) \\ 0 \\ \omega_e\psi_m+(L_{ds}-L_{qs})(\omega_e i_{d2}-pi_{q2}) \end{bmatrix}$$

where u_{d1}, u_{q1}, i_{d1} and i_{q1} are the dq-axis components of the output voltage and output current of the left converter; u_{d2}, u_{q2}, i_{d2} and i_{q2} are the dq-axis components of the output voltage and output current of the right converter; R_{k1}, R_{k2}, L_{k1} and L_{k2} are the parameters of the feeder cables on both sides.

With the three-step switching method, the number of motors on the commutation side increases during the segment transition, and the corresponding motor parameters vary. Taking the SF mode as an example, the voltage equation of the motor corresponding to the departing stator segment is expressed as

$$\begin{bmatrix} u_d \\ u_q \end{bmatrix} = \begin{bmatrix} R_s + R_k + (P_c L_{dis} + L_{dos}) p + pL_k & -\omega_e (P_c L_{qis} + L_{qos}) - \omega_e L_k \\ \omega_e (P_c L_{qis} + L_{qos}) + \omega_e L_k & R_s + R_k + (P_c L_{dis} + L_{dos}) p + pL_k \end{bmatrix} \cdot \begin{bmatrix} i_d \\ i_q \end{bmatrix} + \begin{bmatrix} 0 \\ (\omega_e i_d - p i_q)(P_c L_{dis} + L_{dos} - P_c L_{qis} - L_{qos}) + \omega_e P_c \psi_m \end{bmatrix} \tag{7}$$

The voltage equation of the motor for the incoming stator is expressed as

$$\begin{bmatrix} u_d \\ u_q \end{bmatrix} = \begin{bmatrix} R_s + R_k + [(1-P_c) L_{dis} + L_{dos}] p + pL_k & -\omega_e [(1-P_c) L_{qis} + L_{qos}] - \omega_e L_k \\ \omega_e [(1-P_c) L_{qis} + L_{qos}] + \omega_e L_k & R_s + R_k + [(1-P_c) L_{dis} + L_{dos}] p + pL_k \end{bmatrix} \cdot \begin{bmatrix} i_d \\ i_q \end{bmatrix} + \begin{bmatrix} 0 \\ (\omega_e i_d - p i_q)[(1-P_c) L_{dis} + L_{dos} - (1-P_c) L_{qis} - L_{qos}] + \omega_e (1-P_c) \psi_m \end{bmatrix} \tag{8}$$

Similarly, in the DF mode, the voltage equation of the motor corresponding to the departing stator segment is obtained by combining Equation (5) with Equation (3), whereas that for the incoming stator segment requires the combination of Equation (5) with Equation (4). To directly control the LS-LSM and suppress the circulating current, the *dq*-axis stator current sums and the circulating currents are selected as the new state variables. Meanwhile, the *dq*-axis sums and differences of the output voltages from the two converters are defined as the new input variables. Under the DF mode, Equation (6) can be rewritten as:

$$\begin{aligned} u_{dsum} &= (R_{sum} + L_{dsum} p) i_{dsum} - \omega_e L_{qsum} i_{qsum} + (L_{sub} p + R_{sub}) i_{dsub} - \omega_e L_{sub} i_{qsub} \\ u_{qsum} &= (R_{sum} + L_{qsum} p) i_{qsum} + \omega_e L_{dsum} i_{dsum} + (L_{sub} p + R_{sub}) i_{qsub} - \omega_e L_{sub} i_{dsub} + 2\omega_e \psi_f \end{aligned} \tag{9}$$

where

$$L_{dsum} = 0.5(L_{k1} + L_{k2}) + 2L_{ds},\ L_{qsum} = 0.5(L_{k1} + L_{k2}) + 2L_{qs}$$

$$R_{sum} = 0.5(R_{k1} + R_{k2}) + 2R_s,\ R_{sub} = R_{k1} - R_{k2},\ L_{sub} = L_{k1} - L_{k2}$$

u_{dsum} and u_{qsum} are the sums of the *dq*-axis voltages of the left and right converters, respectively. i_{dsum}, i_{qsum}, i_{dsub} and i_{qsub} represent the total input current of the motor in the *dq*-axis and the differences between the output currents of the two converters, respectively.

4 Proposed Improved ADRC Based on HESO

When the conventional ADRC is applied to the motor current loop control, the *q*-axis current loop is taken as an example, whereas the design methodology for the *d*-axis current loop follows the same principle. The output voltage reference u_{qref} is designated as the control input u, the current reference i_{qref} as the reference signal r, and the *q*-axis current i_q as the output signals y. Defining the state variable $x_1 = i_q$ and the lumped unknown disturbance $f_q = x_2$, the control algorithm is designed as follows

$$\begin{cases} e_1 = (z_1 - x_1) \\ \dot{z}_1 = z_2 - \beta_1 e_1 + b_0 u,\ \dot{z}_2 = -\beta_2 e_1 \\ u_0 = k_p (r - x_1),\ u = u_0 - \dfrac{z_2}{b_0} \end{cases} \tag{10}$$

where z_1 is the estimate of x_1, z_2 is the estimate of x_2, e_1 is the error between z_1 and x_1, k_p is the proportional gain, b_0 is the nominal gain of the input current. For the dynamic system of Equation (10), if the nth rate of change of the disturbance is negligible, the augmented system constructed by introducing n additional states can be expressed as

$$\dot{\boldsymbol{x}} = \boldsymbol{A}\boldsymbol{x} + \boldsymbol{B}u_{qref} + \boldsymbol{C}f_q^{(n)} \tag{11}$$

where

$$\boldsymbol{x} = [x_1\ x_2\ x_3\ \cdots\ x_n]^T_{(n+1)\times 1},\ \boldsymbol{B} = [b_0\ \ 0\ \ 0\ \ \cdots\ \ 0]^T_{(n+1)\times 1}$$

$$\boldsymbol{A} = \begin{bmatrix} 0 & 1 & 0 & \cdots & 0 \\ 0 & 0 & 1 & \cdots & 1 \\ \vdots & \vdots & \vdots & \ddots & \vdots \\ 0 & 0 & 0 & \cdots & 1 \\ 0 & 0 & 0 & \cdots & 0 \end{bmatrix}_{(n+1)\times(n+1)},\ \boldsymbol{C} = [1\ \ 0\ \ 0\ \ \cdots\ \ 0]^T_{(n+1)\times 1}$$

Then, the HESO is designed as

$$\dot{\boldsymbol{z}} = \boldsymbol{A}\boldsymbol{z} + \boldsymbol{B}u_{qref} + \boldsymbol{E}e_1 \tag{12}$$

where

$$\boldsymbol{z} = [z_1\ z_2\ z_3\ \cdots\ z_n]^T_{(n+1)\times 1},\ \boldsymbol{E} = [-\beta_1\ \ -\beta_2\ \ -\beta_3\ \ \cdots\ \ -\beta_n]^T_{(n+1)\times 1}$$

$f_q^{(n)}$ is the nth-order derivate of f_q, z_i (i = 1, 2, ..., n) is the estimate of state variable x_i, n is the extension order, and β_i (i = 1, 2, ..., n) is the observer gain. According to Equation (11) and Equation (12), the observation error equation can be derived as follows

$$\dot{\boldsymbol{e}} = \boldsymbol{A}\boldsymbol{e} + \boldsymbol{E}e_1 - \boldsymbol{C}f_q^{(n)} \tag{13}$$

where $\boldsymbol{e} = [e_1\ \ e_2\ \ e_3\ \ \cdots\ \ e_n]^T_{(n+1)\times 1}$, e_i (i = 1, 2, ..., n) is the error between z_i and x_i .By adopting the bandwidth tuning strategy proposed in [9], the closed-loop poles of the observer can be placed at a common position of $-\omega_o$, where the gain coefficient satisfies

$$\beta_i = \frac{(n+1)!}{i!\,(n+1-i)!}\omega_o^i \tag{14}$$

The corresponding characteristic equation can be written as:

$$D(s) = s^{n+1} + \beta_1 s^n + \beta_2 s^{n-1} + \cdots + \beta_n = (s+\omega_o)^{n+1} \tag{15}$$

To further analyze the characteristics of the ESO with different orders, the transfer function between the observed disturbance z_2 and the actual disturbance f_q is derived as

$$G_z(s) = \frac{z_2}{f_q} = 1 - \frac{s^{n+1} + \beta_1 s^n}{(s+\omega_o)^{(n+1)}} \tag{16}$$

According to Equation (16), the transfer function between the disturbance estimation error e_2 and the actual disturbance f_q is obtained as:

$$G_e(s) = 1 - G_z(s) = \frac{s^{n+1} + \beta_1 s^n}{(s+\omega_o)^{(n+1)}} \tag{17}$$

Under the condition of setting the same bandwidth ω_o, the transfer functions $G_e(s)$ and $G_z(s)$ bode diagrams of the ESOs with different orders are plotted in Figure 5, where ω_o is set to 300 rad/s. It is evident that as the order increases, the dynamic response speed of the ESO is enhanced, and its ability to suppress disturbances is also improved. However, as observed in Figure 5 (b), the magnitude gains of the 3rd-order and 4th-order ESOs exceed 1 near the bandwidth, which implies that higher-order ESOs are more sensitive to measurement noise. Therefore, the selection of the ESO order requires a comprehensive trade-off between disturbance rejection capability and robustness to noise.

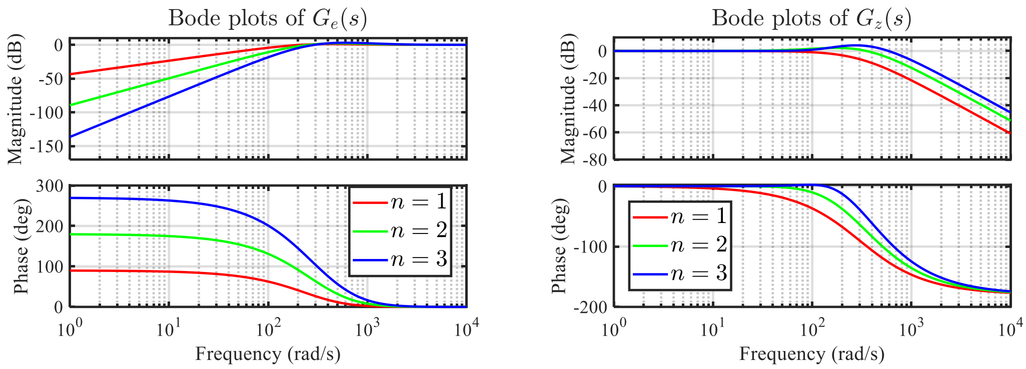

(a) (b)

Figure 5: Bode plots of G_e(s) and G_z(s) with different orders ESO.

This study augments the state vector with three additional state variables and employs a fourth-order ESO to observe the disturbances in the current loop. The transfer function between the observed disturbance z_2 and the actual disturbance f_q for the fourth-order ESO is given by

$$G_z(s) = \frac{\beta_2 s^2 + \beta_3 s + \beta_4}{s^4 + \beta_1 s^3 + \beta_2 s^2 + \beta_3 s + \beta_4} \tag{18}$$

Using the conventional bandwidth method, the parameters of Equation (18) are tuned as follows

$$\beta_1 = 4\omega_o,\ \beta_2 = 6\omega_o^2,\ \beta_3 = 4\omega_o^3,\ \beta_4 = \omega_o^4 \tag{19}$$

The control block diagram of the current loop based on the fourth-order ESO is depicted in Figure 6. If the lumped disturbance can be accurately estimated and compensated, the original system degenerates into a pure integrator. In this case, the closed-loop transfer function can be approximated as:

$$\frac{\boldsymbol{i}_{dq}}{\boldsymbol{i}_{dq}^{ref}} = \frac{k_p}{s + k_p} \tag{20}$$

Thus, the bandwidth of the closed-loop system is determined by the proportional gain k_p. Specifically, once k_p is fixed, the frequency-domain characteristics of $G_z(s)$ directly govern the system's disturbance rejection and noise attenuation performance.

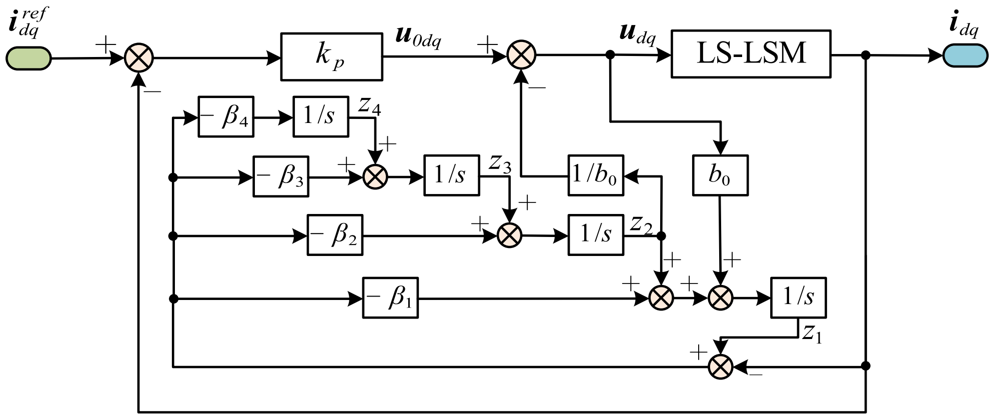

Figure 6: Structure diagram of the ADRC based on HESO.

5 Simulation Results

To verify the effectiveness of the proposed control scheme, the high-speed maglev traction system under SF mode and DF mode is simulated. The three-step switching method is adopted for power supply commutation. The LS-LSM parameters are taken as shown in Table 1. The overall system structure diagram is shown in Figure 7. The three-step switching method decouples the traction process into two phases: the steady-state operation and the changeover process. During steady-state operation, the train traction force is jointly provided by two motors. In contrast, during changeover process, the traction characteristic is equivalent to the combined effect of three motors. In this study, three sets of independent current loops and modulation strategies with identical parameters are constructed. The traction control system employs a single shared speed loop and performs online allocation of the q-axis current references for each motor based on the stator-mover coupling coefficients. This ensures a constant amplitude of the total traction force before and after the changeover, thus achieving a smooth traction force transition.

Parameters	Value	Parameters	Value
Stator resistance R_s	436.176mΩ	Feeder cable resistance R_k	58.33mΩ/km
d-axis inductance L_{ds}	3.9153mH	Feeder cable inductance L_k	0.0713mH/km
q-axis inductance L_{qs}	3.4653mH	Stator pole pitch τ	0.258m
Excitation flux ψ_m	4.455Wb	The gross weight of the train	306.9t

Table 1: Parameters of the LS-LSM.

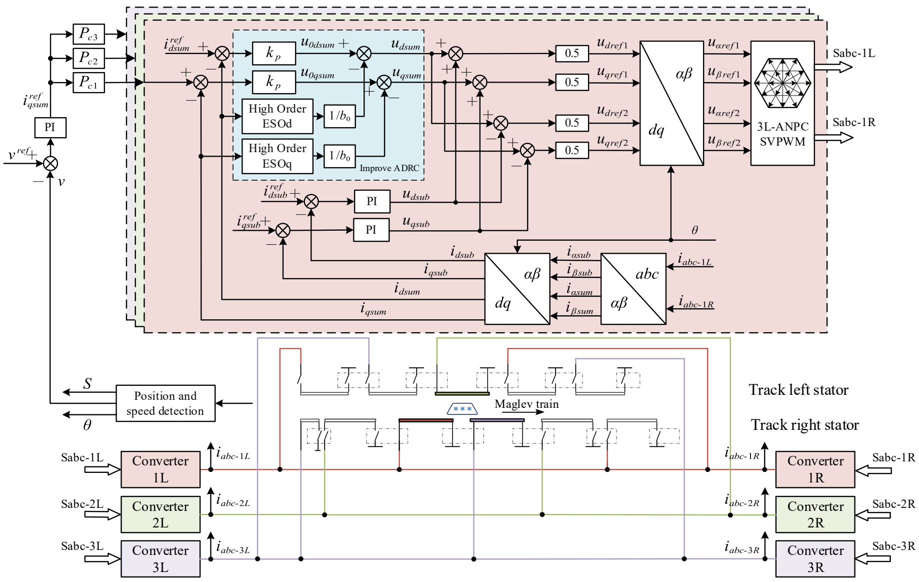

Figure 7: Structure diagram of the improved ADRC for the LS-LSM under three-step power supply switching method.

5.1 LS-LSM Segment Switching Characteristics

The train operation condition is set as an acceleration–deceleration process covering 0 km/h to 600 km/h and back to 0 km/h. Figure 8 presents the dynamic response curve of the speed loop under this full operating condition. It can be observed that the actual speed accurately tracks the speed reference command, demonstrating excellent dynamic tracking performance. Figure 9 illustrates the *dq*-axis inductance variation curves of different motors in the high-speed maglev simulation model based on the three-step switching method. During the changeover process, the inductance variation follows the linear trend obtained from the finite element simulation results in Figure 4. In the steady-state non-transition phase, only two motors maintain their rated inductance values, while the inductance of the third motor consists solely of the uncoupled stator segment inductance, thus exhibiting a pure resistance–inductance characteristic.

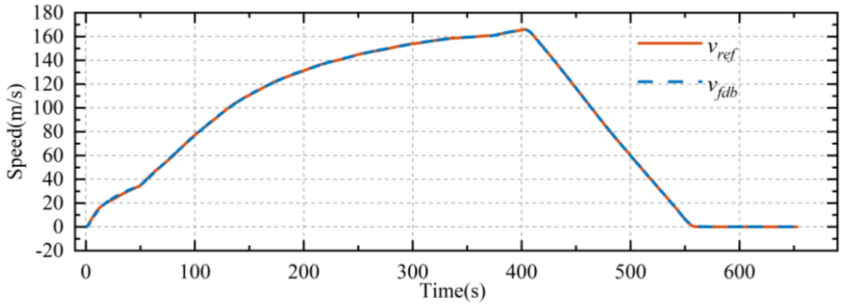

Figure 8: Dynamic tracking performance of the speed loop.

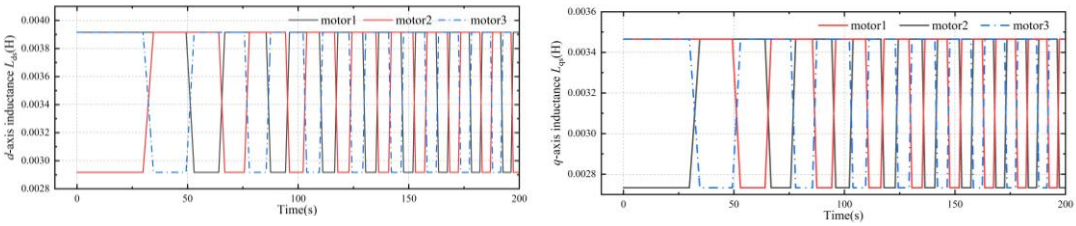

(a) *d*-axis inductance (b) *q*-axis inductance

Figure 9: Change of different motor parameters.

Figure 10 compares the traction force waveforms of the train during the full acceleration–deceleration process of 0–600–0 km/h under different power supply switching methods. It can be seen that the traction force amplitude of the two-step method drops sharply by 50% at the moment of segment transition, whereas the traction force output of the three-step method remains smooth over the entire speed range. Benefiting from the advantage of traction force loss-free of the three-step method, the train's acceleration performance is significantly boosted. Compared with the two-step method, it can transit faster to the operating phases including SF/DF power supply mode switching, acceleration/deceleration switching and parking.

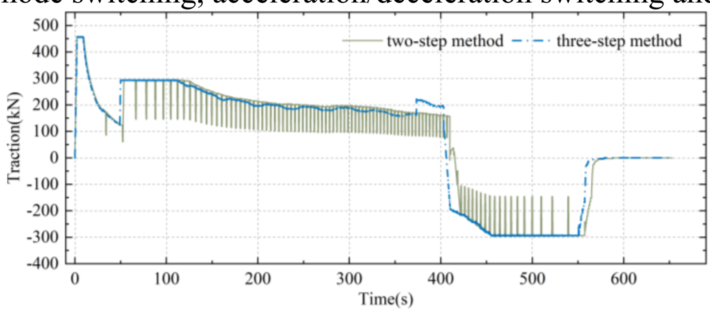

Figure 10: Traction waveform of different power supply switching strategies.

5.2 Simulation Results of the Current Loop under Different Control Strategies

Figure 11 presents the current loop response characteristics of Motor 1 with different current control strategies over the full speed range of 0–600–0 km/h. A comparison is made between the conventional PI control in Figure 11(a) and the ADRC control proposed in this study in Figure 11 (b), with the PI parameters set as k_p = 7 and k_i = 80, and the parameters of the improved ADRC set as k_p = 7 and ω_o = 300. In Figure 11 (b), the actual current exhibits excellent tracking performance of the reference current, which verifies the effectiveness of the proposed ADRC algorithm under full operating conditions. Figure 12 shows the local current response characteristics under different control strategies. The motor parameters present a remarkable time-varying characteristic in the segment transition interval; the conventional PI control in Figure 12 (a) suffers from insufficient robustness, which leads to a severe *q*-axis current overshoot of Motor 1 during the changeover process and thus deteriorates the control performance of the system current loop. Whereas, the ADRC control strategy proposed in this study is adopted in Figure 12 (b), and by virtue of the real-time estimation and compensation of internal and external disturbances by the high-order ESO, the current overshoot and steady-state error are effectively eliminated, achieving favorable tracking of the reference current.

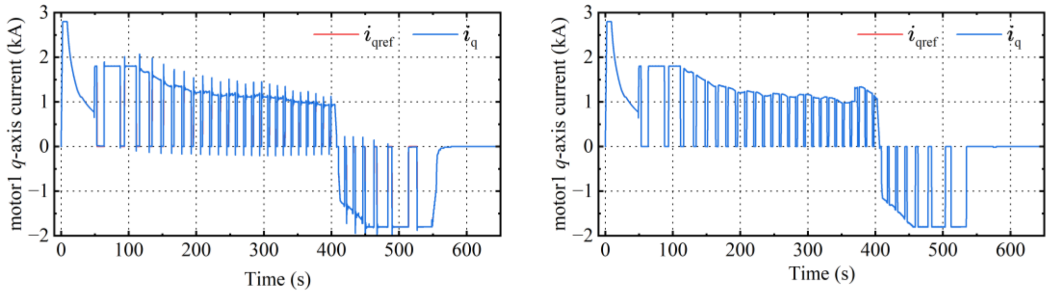

(a) PI (b) proposed ADRC

Figure 11: Simulation results of the q-axis current response.

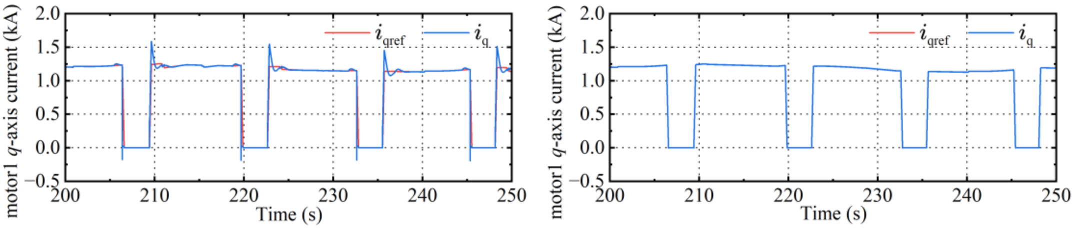

(a) PI (b) proposed ADRC

Figure 12: q-axis current during the changeover process.

6 Conclusion

A 3D finite element model of the LS-LSM is established in this study, which reveals the time-varying characteristics of motor inductance during the changeover process. Based on the coupling coefficient, the motor model under the three-step switching method is revised and refined; meanwhile, the ADRC scheme based on HESO is designed for the current loop to enhance the system's ability to suppress disturbances caused by parameter mismatches. Simulation results demonstrate that, in comparison with the conventional PI control, the proposed method effectively improves the dynamic response and steady-state accuracy of the current loop, and exhibits excellent robustness against motor parameter mismatches.

Acknowledgements

This research was funded by the National Natural Science Foundation of China under Grant 52302458.

References

[1] R. Hellinger and P. Mnich, "Linear motor-powered transportation: History, present status, and future outlook," Proc. IEEE, vol. 97, no. 11, pp. 1892–1900, Nov. 2009.

[2] H.-W. Lee, K.-C. Kim, and J. Lee, "Review of maglev train technologies," IEEE Trans. Magn., vol. 42, no. 7, pp. 1917–1925, Jul. 2006.

[3] Liu Jinxin, Ge Qiongxuan, Wang Xiaoxin, et al. Traction-system research for high-speed maglev based on double-end supply[J]. Advanced Technology of Electrical Engineering and Energy, 2015, 34(6): 16-21, 44.

[4] X. Cao, Q. Ge, J. Zhu, G. Kong, B. Zhang and X. Wang, "Improved Sliding Mode Traction Control Combined Sliding Mode Disturbance Observer Strategy for High-Speed Maglev Train," in IEEE Transactions on Power Electronics, vol. 38, no. 1, pp. 827-838, Jan. 2023.

[5] J. Chen, Y. Fan, M. Cheng, Q. Zhang and Q. Chen, "Parameter-Free Ultralocal Model-Based Deadbeat Predictive Current Control for PMVMs Using Finite-Time Gradient Method," in IEEE Transactions on Industrial Electronics, vol. 70, no. 6, pp. 5549-5559, June 2023.

[6] Zhu Jinquan, Ge Qiongxuan, Sun Pengkun, et al. Traction-system research of high-speed maglev based on active disturbance rejection control[J]. Transactions of China Electrotechnical Society, 2020, 35(5): 1065-1074.

[7] Z. Gao, “Scaling and bandwidth-parameterization based controller tuning,” in Proc. Amer. Control Conf., 2003, pp. 4989–4996.

[8] W. Chen, Q. Ge, B. Zhang, J. Zhu and M. Zhao, "Traction Control Strategy of High-Speed Maglev Train Considering Inductance Asymmetry," 2025 IEEE 8th International Electrical and Energy Conference (CIEEC), Changsha, China, 2025, pp. 827-833.

[9] Y. Yan, Z. Sun, and S. Li, “Disturbance rejection control method based on composite disturbance observer for permanent magnet synchronous motor,” in Proc 41st Annu. Conf. IEEE Ind. Electron. Soc., 2015, pp. 3137–3142.

[10] Shanfeng Zhu, Wenxin Huang, et al., "Robust Speed Control of Electrical Drives With Reduced Ripple Using Adaptive Switching High-Order Extended State Observer," in IEEE Transactions on Power Electronics, 37(2): 2009-2020, 2022.